

Article

Deposition of Nickel-Based Superalloy Claddings on Low Alloy Structural Steel by Direct Laser Deposition

André Alves Ferreira ^{1,2,*} , Rui Loureiro Amaral ², Pedro Correia Romio ¹ , João Manuel Cruz ³, Ana Rosanete Reis ^{1,2} and Manuel Fernando Vieira ^{1,2,*} 

¹ Faculty of Engineering, University of Porto, R. Dr. Roberto Frias, 4200-465 Porto, Portugal; pedro.romio@gmail.com (P.C.R.); areis@inegi.up.pt (A.R.R.)

² LAETA/INEGI—Institute of Science and Innovation in Mechanical and Industrial Engineering, R. Dr. Roberto Frias, 4200-465 Porto, Portugal; ramaral@inegi.up.pt

³ SERMEC-Group, R. de Montezelo 540, 4425-348 Porto, Portugal; joaocruz@sermecgroup.pt

* Correspondence: andreferreira@fe.up.pt (A.A.F.); mvieira@fe.up.pt (M.F.V.); Tel.: +351-910-461-480 (A.A.F.)

Abstract: In this study, direct laser deposition (DLD) of nickel-based superalloy powders (Inconel 625) on structural steel (42CrMo4) was analysed. Cladding layers were produced by varying the main processing conditions: laser power, scanning speed, feed rate, and preheating. The processing window was established based on conditions that assured deposited layers without significant structural defects and a dilution between 15 and 30%. Scanning electron microscopy, energy dispersive spectroscopy, and electron backscatter diffraction were performed for microstructural characterisation. The Vickers hardness test was used to analyse the mechanical response of the optimised cladding layers. The results highlight the influence of preheating on the microstructure and mechanical responses, particularly in the heat-affected zone. Substrate preheating to 300 °C has a strong effect on the cladding/substrate interface region, affecting the microstructure and the hardness distribution. Preheating also reduced the formation of the deleterious Laves phase in the cladding and altered the martensite microstructure in the heat-affected zone, with a substantial decrease in hardness.

Keywords: direct laser deposition; Inconel 625; parametrisation; microstructure; microhardness; preheating



Citation: Ferreira, A.A.; Amaral, R.L.; Romio, P.C.; Cruz, J.M.; Reis, A.R.; Vieira, M.F. Deposition of Nickel-Based Superalloy Claddings on Low Alloy Structural Steel by Direct Laser Deposition. *Metals* **2021**, *11*, 1326. <https://doi.org/10.3390/met11081326>

Academic Editors: Atilla Ertas and Adam Stroud

Received: 16 July 2021

Accepted: 20 August 2021

Published: 22 August 2021

Publisher's Note: MDPI stays neutral with regard to jurisdictional claims in published maps and institutional affiliations.



Copyright: © 2021 by the authors. Licensee MDPI, Basel, Switzerland. This article is an open access article distributed under the terms and conditions of the Creative Commons Attribution (CC BY) license (<https://creativecommons.org/licenses/by/4.0/>).

1. Introduction

The laser-based additive manufacturing (LBAM) technologies applied in the production and repair of industrial components emerged in the late 1990s. Their use continues to extend to many industrial sector applications for components that operate in extreme conditions. LBAM technologies are unique and versatile in the manufacturing of parts with complex geometry, functionally graded or customised, producing an improvement in properties that can be used for a variety of industrial applications, such as within the aerospace, metallurgy, energy, and automotive industries [1,2]. Direct laser deposition (DLD) is an LBAM technology used for the additive manufacturing of metal parts, reconstructions, and repairs. DLD consists of the supply, through a nozzle, of metallic powder (or wire) processed by a focused laser, creating a melt pool on the surface of a metallic substrate. Several processing variables directly or indirectly affect the quality and structural integrity of components, dictated by solidification and metallurgical bonding [3].

DLD involves interactions between the laser beam, powder, and substrate in an environment with local protection from inert gas. Laser power, scanning speed, beam size, and powder feed rate are parameters that play a dominant role in cladding geometry (height, width, and length), dilution, and metallurgical properties. Clad overlapping, gas flow rate, powder flow profile, powder quality (size, shape, and density), and preheating are important secondary parameters [4,5].

The success of DLD depends on the selection of processing conditions that guarantee an effective bonding of the deposited material. This proper bonding produces adequate thermal delivery control, dense layers, a small heat-affected zone (HAZ), low dilution, minimal distortion, and good surface quality, with an attractive set of mechanical properties as well as resistance to wear and corrosion [6–8]. A controlled DLD process can replace conventional processes (i.e., electric arc welding and thermal spraying) in order to repair industrial components. Traditional approaches present drawbacks in component repairs, such as the time required, the limited thickness of the deposition layers, the low metallurgical bond, the formation of porosities and cracks, and the distortion of substrates (caused by overheating of the components). Therefore, it is of industrial interest to develop high-efficiency and -precision repair technologies to increase component life.

This additive manufacturing technology is considered the best strategy for reconstructing and repairing damaged components in terms of environmental benefit and economic feasibility. However, it is regarded as a complex process due to uncertainties in the quality and reliability of recovered industrial components [9], requiring further investigation to consolidate the results reported in this area. Although the equipment cost is high, DLD has successfully repaired dies, moulds, turbines, and gears. Adaptability for automation, ease of assembly of the laser on a CNC machine or robotic arm, and lower post-processing requirements are additional advantages of the DLD process [10,11].

DLD still has a way to go for broader industrial applications. Theoretical and experimental studies have developed relevant information about DLD; however, there are still many challenges, such as process optimisation, 3D reconstruction of highly complex structures, and substrate preheating effects, which need to be clarified. The production of wear-resistant claddings on low and medium carbon steel substrates is an application that can have many industrial applications, both in component repair and protective coating with a thick resistant layer.

Nickel-based superalloys are an excellent option for producing this wear-resistant layer. These alloys have been adopted in multiple applications due to their properties, such as mechanical behaviour at high temperatures, hardness, mechanical resistance, and good fatigue resistance, creep, and corrosion [12,13]. These properties are conferred by the structure and chemical composition of the alloy, mainly by elements such as molybdenum (Mo) and niobium (Nb), which form a solid solution in a nickel–chromium matrix [14]. While conventional manufacturing with these high-performance alloys has been difficult due to excessive tool wear and low material deposition rates, LBAM technologies can overcome these constraints, improving delivery times, and reducing manufacturing costs [15].

The use of nickel-based superalloys in DLD must consider the high cooling rates of the process, promoted by the localised thermal delivery induced by the laser beam, which can lead to the formation of metastable phases and the segregation of elements. These microstructural effects reduce the toughness and hardness of the coated components [16–19]. Preheating (PHT) is essential to control the cooling rate, minimising this effect. Increasing PHT temperature promotes the growth of the melt pool (depth and width), melting more substrate, thus increasing dilution [20–24]. PHT also prevents cladding delamination or cracking and reduces distortion and residual stresses due to the lower thermal gradient between the cladding and substrate [7,25,26].

In this study, Inconel 625, a nickel-based superalloy, powder was deposited on 42CrMo4 steel, while the process parameters were varied. 42CrMo4 steel is often used to produce components, such as gears and main shafts, and Inconel 625 is employed in the repair/remanufacturing of these components by SERMEC Group. Single layers were produced to evaluate the metallurgical bonding with a substrate; the influence of several processing parameters, such as laser power, scanning speed, and powder feed rate on the cladding quality, was evaluated considering the absence of cracks and structural imperfections. Preheating was performed on an optimised cladding condition in order to moderate

the microstructure and mechanical responses. Microhardness profiles of claddings were obtained and correlated with the microstructures.

2. Materials and Methods

2.1. DLD System Setup

A laser system, LDF 3000–100, was used to produce DLD claddings. The system has a high-power fibre-coupled laser diode (wavelength 900–1030 nm, depending on the power), with a nominal beam power of 6000 W. The machine concept is a KUKA KR90 R3100 industrial robot, based on a 6-axis industrial robot. All axes are connected to the robot and laser control units, which command the temperature of the melt pool as well as the laser power. The powder was fed during the deposition process by a coaxial feeding system, as illustrated in Figure 1. The substrate was preheated (PHT) to 300 °C with a manual gas system. The temperature control of the preheated substrate was done by a digital pyrometer, for verification of the uniformity of the substrate surface temperature distribution. Preheating is intended to decrease the cooling rate in the melt pool and HAZ regions as well as eliminate moisture. Tests were performed on substrates after the production of clads, with and without PHT, to evaluate susceptibility to cracking and eventual formation of metastable phases.

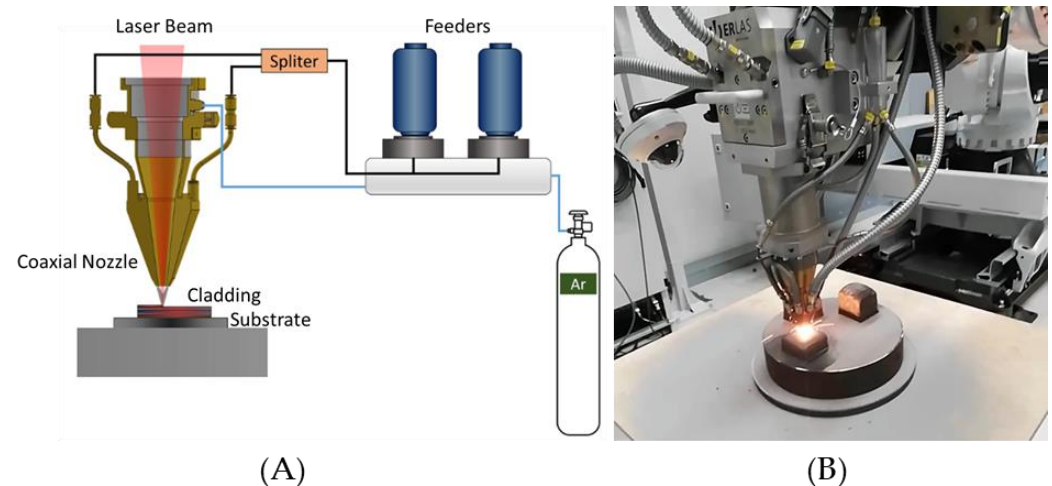


Figure 1. (A) Schematic representation of the direct laser deposition system with two feeders; (B) system in operation.

2.2. Feedstock Powder and Substrate

A nickel-based superalloy (MetcoClad 625 from Oerlikon), similar to Inconel 625, produced by the gas-atomised process, was used in this study. This powder was developed specifically for laser processing and presents a spherical morphology as well as particle sizes ranging between 45 and 90 μm . Figure 2 shows scanning electron microscopy (SEM) images of the morphology of the MetcoClad 625 powder.

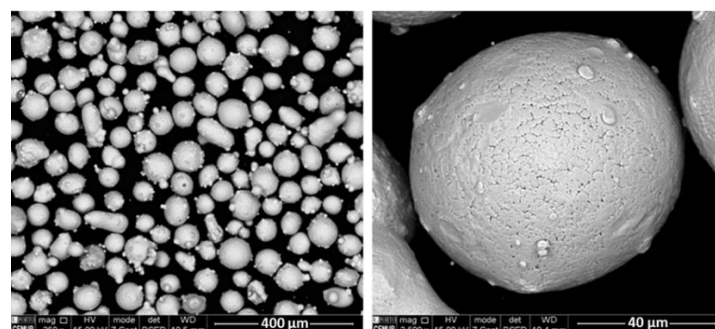


Figure 2. SEM images of MetcoClad 625 powder.

42CrMo4 steel, in the quenched and tempered condition, was used as a substrate for the DLD deposition. Specimens with dimensions of 100 mm × 120 mm × 15 mm were prepared for depositions. This steel is classified as a low alloy structural steel with high mechanical strength and toughness as well as good fatigue resistance and machinability, being widely used in the manufacturing of critical industrial components, such as gears, automotive components, wing generators, and drilling joints for deep wells [27]. Its mechanical and chemical properties are described in standard EN 10,269 [28]. The chemical composition of the MetcoClad 625 (M625) powder and 42CrMo4 steel are shown in Table 1.

Table 1. Chemical composition of M625 powder and 42CrMo4 steel (wt.%).

| Material | Ni | Cr | Mo | Nb | Si | Mn | C | Fe |
|----------|------|------|-----|-----|-----|-----|-----|------|
| M625 | 60.8 | 21.3 | 9.2 | 4.6 | - | - | - | 4.1 |
| 42CrMo4 | - | 1.1 | 0.2 | - | 0.3 | 0.7 | 0.4 | 97.3 |

2.3. Process Parameters

The main process parameters (laser power, scanning speed, and feed rate) were considered to evaluate the effect of processing conditions on clads. The evaluation of the clad quality depends on clad characteristics, namely, absence of cracks or pores, good metallurgical bond (interfaces without microcracks, pores, and fragile phases, exhibiting good wettability), and dilution between 15 and 30%. The values of the tested parameters are shown in Table 2. All results are representative of single-layer samples. The terminology ILP_SS_FR was used to identify the samples, being I—M625 powder (Inconel powder); LP—laser power (kW); SS—scanning speed (mm/s); FR—feed rate (g/min). Eighteen combinations of different processing conditions were tested, with and without preheating (see Table 3). Before deposition, the substrates were cleaned with pure acetone.

Table 2. Process parameters tested for M625 deposition on 42CrMo4 substrate.

| Process Parameters | Values |
|---------------------|--------------------------------|
| Laser power (LP) | 1.0, 1.5, 2.0, 2.5, and 3.0 kW |
| Scanning speed (SS) | 2.0, 4.0, 6.0, and 10.0 mm/s |
| Feed rate (FR) | 10, 15, and 20 g/min |

In all tests, a spot size of 2.5 mm and an offset in the Z-axis of 0.2 mm were used. High-purity argon (99.99%), with a 5.5 L/min flow rate, was used as the shielding gas for minimising contamination of the melt pool during the DLD process. Samples with and without PHT were cooled in air.

2.4. Mechanical and Microstructural Characterisation

Samples from each deposition were cut for microstructural and mechanical characterisation using a metallographic cut-off machine with refrigeration in order to avoid substrate and cladding overheating. Samples were mounted in resin and polished down to a 1 µm diamond suspension. Kalling's N^o. 2 chemical etching (CuCl₂—5 g, hydrochloric acid—100 mL, and ethanol—100 mL) was used to reveal the microstructures.

The measurements of the height, depth, and width of the claddings produced by the DLD technique were performed using a Leica DVM6 A 2019 digital microscope (DM) (Wetzlar, Germany). The Leica DM 4000 M optical microscope (OM) (Wetzlar, Germany) allowed for a microstructural analysis at low magnifications to evaluate, for example, the size of the heat-affected zone. A scanning electron microscope, FEI Quanta 400 FEG (ESEM, Hillsboro, OR, USA), equipped with energy-dispersive X-ray spectroscopy (EDX) (EDAX Genesis X4M, Oxford Instrument, Oxfordshire, UK) and electron backscatter diffraction (EBSD) (EDAX-TSL OIM EBSD, Mahwah, NJ, USA) was used for higher magnification observation and phase identification. For EBSD evaluation, the samples went through an additional polishing step, using a 0.06 µm silica colloidal suspension, for a superior surface

finish and to remove polishing-induced plastic deformations, allowing Kikuchi patterns to be obtained [29]. EBSD allows for the obtaining of information on microstructural characteristics with a small interaction volume and a high resolution, for which TSL OIM Analysis 5.2 software was used. For all raw data obtained by EBSD, a dilatation clean-up routine was performed, with a grain tolerance angle of 15° and a minimum grain size of 10 points.

Quantitative image analysis was employed on optical images using the ImageJ software, version 1.51p (National Institutes of Health, Bethesda, MD, USA).

Vickers microhardness tests gave the mechanical characterisation. The tests were performed using a test force of 300 g for 15 s in a Struers Duramin 5 (Struers Inc., Cleveland, OH, USA) Vickers hardness tester. Each hardness value corresponds to the average of three indentations.

3. Results and Discussion

3.1. Processing Effects

The quality of cladding was first evaluated by inspection with a digital microscope (DM). The microstructural analysis of all the claddings produced did not detect cracks, pores, or inclusions of significant dimensions, an essential requirement for obtaining high-performance deposits.

SEM characterisation confirmed the observations made by the DM. Figure 3 shows an SEM image of the cross-section of an M625 clad deposited on 42CrMo4 steel, representing the geometric aspects of cladding: height (h), width (w), depth (d), clad area (AC), melting area (AM), and wetting angle (θ). These geometric aspects were measured on all claddings using the ImageJ software. The results are shown in Table 3.

Table 3. Dimensional analysis of claddings produced by DLD.

| Sample | Cladding Dimensional Analysis | | | | | | |
|------------|-------------------------------|-----------|-----------|-----------------|--------------------------|--------------------------|----------|
| | W (mm) | H (mm) | D (mm) | θ (°) | AC (mm ²) | AM (mm ²) | D (%) |
| I1_2_15 | 2.79 | 3.07 | 0.25 | 121 | 9.9 | 0.3 | 2.6 |
| I1_6_15 | 3.07 | 1.22 | 0.06 | 64 | 3.0 | 0.0 | 1.3 |
| I1.5_10_10 | 3.09 | 0.71 | 0.43 | 47 | 5.8 | 2.1 | 26.5 |
| I1.5_10_15 | 3.11 | 1.03 | 0.23 | 64 | 2.3 | 0.2 | 7.3 |
| I2_2_15 | 3.62 | 3.66 | 1.28 | 107 | 15.2 | 3.0 | 16.6 |
| I2_4_15 | 3.50 | 2.47 | 1.12 | 88 | 7.2 | 2.4 | 25.0 |
| I2_6_10 | 3.38 | 1.39 | 1.16 | 53 | 3.3 | 2.3 | 40.6 |
| I2_6_15 | 3.61 | 1.47 | 0.51 | 65 | 4.5 | 1.3 | 22.0 |
| I2_6_20 | 3.63 | 1.71 | 0.56 | 74 | 4.9 | 1.2 | 19.5 |
| I2_10_10 | 3.20 | 1.20 | 0.72 | 58 | 2.7 | 1.1 | 29.1 |
| I2_10_15 | 3.36 | 0.81 | 0.88 | 40 | 1.9 | 1.5 | 45.1 |
| I2.5_10_10 | 3.33 | 0.86 | 1.04 | 49 | 2.1 | 2.3 | 52.1 |
| I2.5_10_15 | 3.36 | 1.23 | 1.00 | 51 | 2.9 | 1.9 | 39.8 |
| I3_2_15 | 5.05 | 3.40 | 2.06 | 99 | 15.4 | 6.6 | 29.9 |
| I3_4_15 | 4.64 | 2.06 | 0.89 | 70 | 7.5 | 2.5 | 25.3 |
| I3_6_10 | 3.89 | 1.85 | 1.08 | 74 | 6.2 | 2.8 | 30.8 |
| I3_6_15 | 4.71 | 0.78 | 0.68 | 37 | 2.8 | 2.6 | 48.0 |
| I3_6_20 | 3.94 | 1.55 | 1.34 | 69 | 4.6 | 3.3 | 41.6 |

This analysis of the geometry of the single-track deposits is critical as it provides information on process yield and cladding performance. For example, the contact angle is an essential parameter in assessing the quality of the cladding [30,31]. Higher beads can promote low wettability during the deposition of multi-tracks, hindering overlapping and generating discontinuities in the hatch spacing of the overlapping deposits, thus facilitating crack propagation. Typically, a contact angle greater than 90° is associated with lower-quality claddings [32]. Table 3 shows that depositions with higher heights have a high contact angle, as samples I1_2_15, I2_2_15, and I3_2_15 demonstrate.

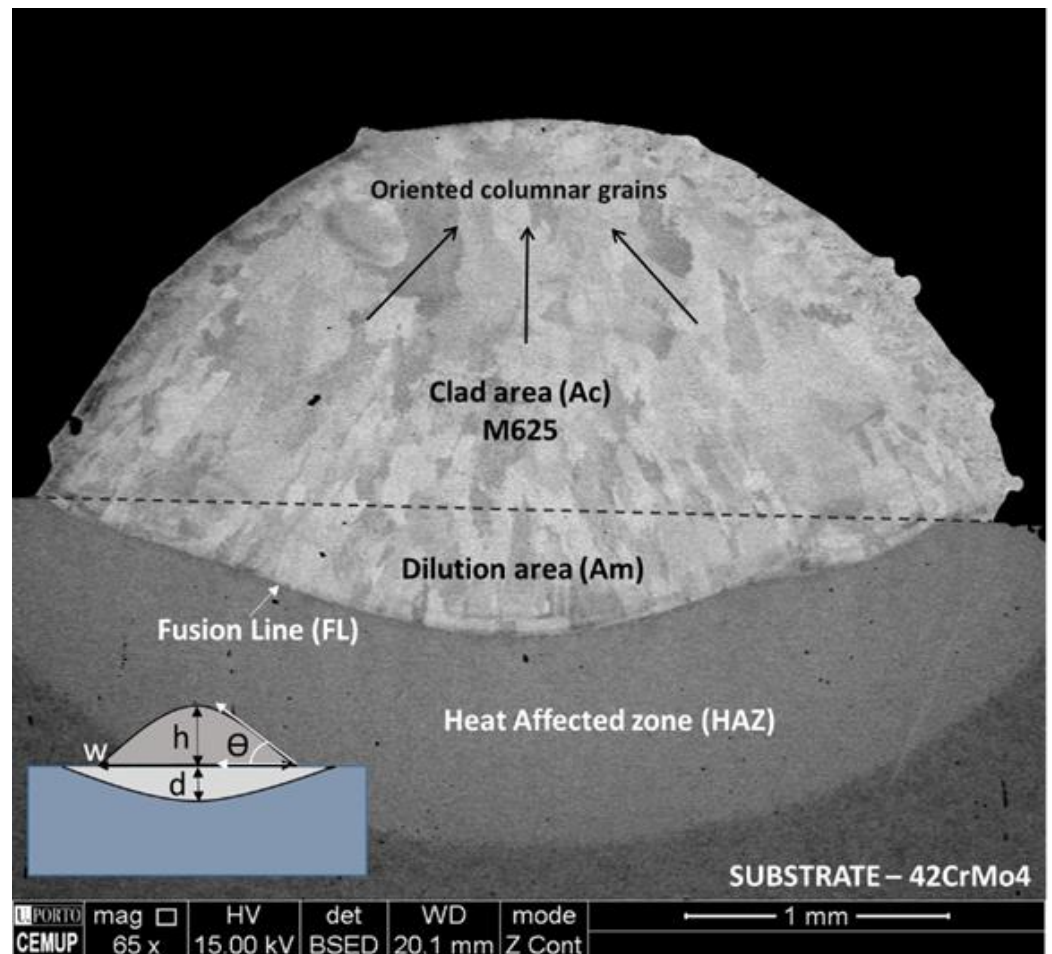


Figure 3. Cross-section of a single layer of M625 deposited on 42CrMo4: d—depth; h—height; w—width; θ —contact angle; AC—clad area; and AM—melting area.

The results presented in Table 3 show that the analysed processing parameters (laser power, scanning speed, powder feed rate, and preheating) strongly influence the production of the cladding and its bonding to the substrate. The selection of a processing window that guarantees a metallurgically bonded clad with good material yield is a fundamental task. This selection is difficult since the mutual interaction of the various parameters is complex. Thus, it is common to apply combined parameters in the DLD process to obtain a more accurate relationship between processing parameters and the clad characteristics [33].

One of the most used complex parameters is powder deposition density (PDD), which expresses the combined effect of feed rate, scanning speed, and laser spot size (φ) (Equation (1)) [34–36]. Figure 4 exposes the linear growth of the cladding area with the increase in the PDD parameter.

$$\text{PDD (g/mm}^2\text{)} = \text{FR}/(\text{SS} \times \varphi) \quad (1)$$

This parameter shows that by increasing the feed rate or decreasing the scanning speed, we can obtain claddings with a larger area, which was expected since both situations result in more powder supply in the same period of time. PDD is a valuable parameter, but this relationship is only valid for the cladding area and not for the total area of the deposit, including the area of the substrate that has been melted. This last area is vital because it affects the quality of the cladding.

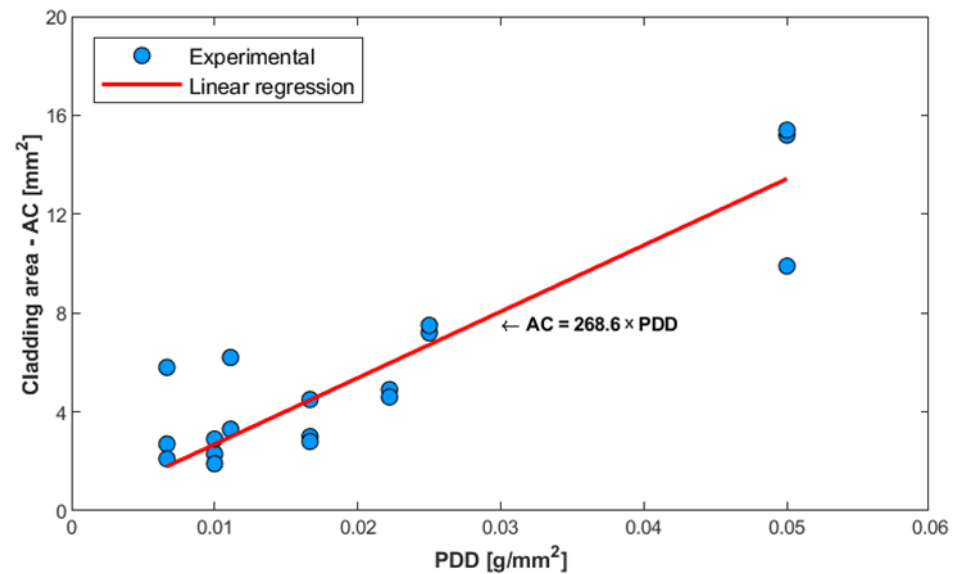


Figure 4. Dependence of cladding area on the value of the PDD complex parameter.

Additionally, with the measured areas (Table 3), it was possible to calculate the dilution, which quantifies the relative amount of melted substrate during laser processing, according to Equation (2).

$$\text{Dilution (\%)} = \text{AM}/(\text{AC} + \text{AM}) \times 100 \quad (2)$$

A dilution ratio between 15 and 30% is sufficient to allow a good metallurgical bond between the substrate and the cladding. Higher dilution, which means a greater melting of the substrate, is undesirable since it reduces the deposition yield and induces considerable changes in the chemical composition of the deposited material, modifying the expected properties of the cladding.

The results obtained, and presented in Table 3, indicate that dilution increases with increased laser power, keeping the other processing variables constant. A laser power of 1.5 kW is enough to guarantee a dilution higher than 15% for almost all conditions (the only exception is the I1.5_10_15 sample).

Despite this apparent direct relation between laser power and dilution, the effect of other critical processing variables, namely the scanning speed and the feed rate, makes the establishment of relationships between processing condition and dilution complex. To overcome this difficulty, it is common to apply complex parameters, empirically adjusted, to the clad/substrate set under analysis to define the processing window [33,37,38].

Figure 5 shows a process window map, which associates laser power with the scanning speed and feeding rate ratio, as well as the dilution that is correlated with the laser power through complex parameter $LP (SS/FR)^{0.5}$; it is represented by two curves, one for 15% and the other for 30%. Additionally, as was also considered in the map, a vertical line that corresponds to the acceptable limit for the wetting angle is present.

As seen in Figure 5, the shaded area, delimited by the previous conditions (dilution range, acceptable wetting angle, and process parameters), reveals the desirable practical manufacturing processing window of Inconel 625. In addition, the dilution increases proportionally with the increase in laser power and decreases with the ratio between scanning speed and feeding rate [39]. The flow of liquid metal in the melt pool is dominated by Marangoni's convection effect, caused by the surface tension gradient. As the temperature of the substrate increases, this effect becomes more evident. However, in practice, the surface tension gradient (γ) $d\gamma/dT$ depends on both temperature (T) and composition. In this case, the most significant influence factor is the thermal gradient promoted between laser beam and substrate, as Le et al. [40] demonstrated, where the increase in the substrate temperature becomes more evident.

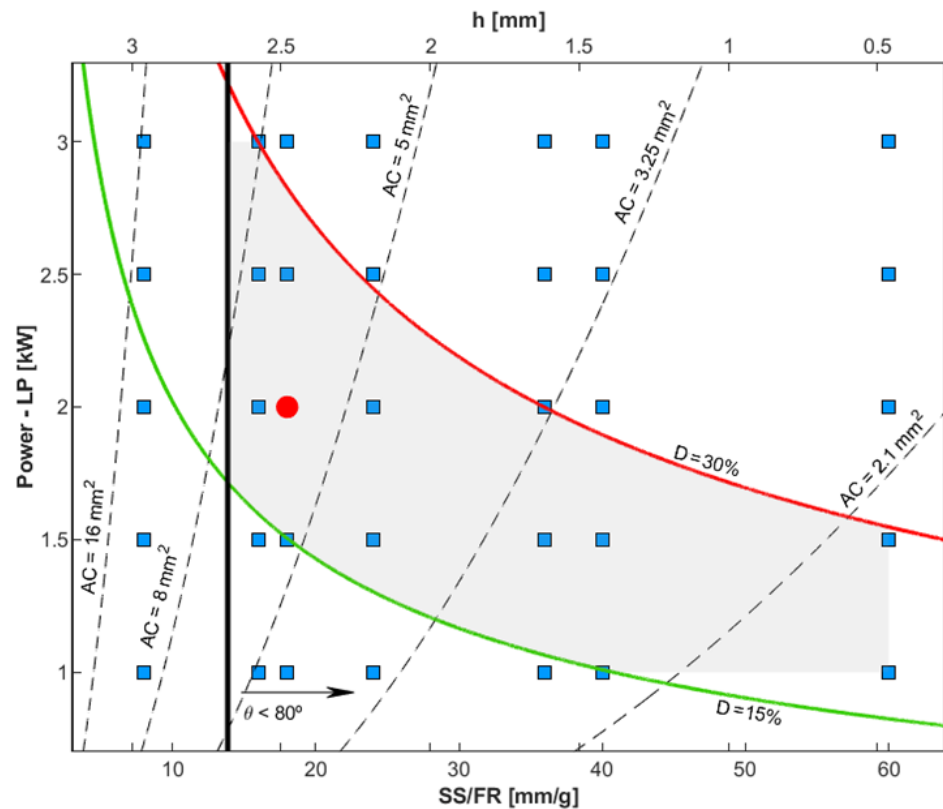


Figure 5. DLD process window map of M625 for additive manufacturing of single tracks. Red point represents the experimental I2_6_20 condition.

Laser power control allows the required good metallurgical integrity and dilution to be achieved [41], producing a cladding with a good metallurgical bond and uniform properties. Increasing the power of the laser promotes increased energy density as well as greater dilution and mixing between the substrate and the deposited powder, which is characteristic of the laser alloy process [42].

Considering the analyses performed, the I2_2_15, I2_4_15, I2_6_15, I2_6_20, I2_10_10, I3_2_15, and I3_4_15 conditions showed dilutions within the established range, between 16.6% and 29.9%, but a lower dilution value is preferable. Nevertheless, the I2_2_15, I2_4_15, and I3_2_15 samples presented poor wettability angles (107° , 88° , and 99° , respectively) that may lead, in future, to claddings with overlapping defects between strands. On the other hand, the four remaining conditions presented good wetting angles, but taking into account not only the quality of the process but also its efficiency, condition I2_6_20 (Figure 5 red point) is the only one that allows for the possibility of manufacturing a larger cladding area and consequently a higher cladding height, which has an inverse linear relationship with the SS/FR ratio. Considering this evaluation, the I2_6_20 condition will be used to perform the analyses throughout the following sections.

3.2. Microstructures and Mechanical Characterisation of the DLD Samples

Figure 6 shows the cladding microstructure formed adjacent to the substrate by the deposition of M625 on 42CrMo4 steel. This microstructure consists of columnar grains, mainly dendrites, and cellular morphologies in a few regions.

As shown in Figure 6B, on solidification a continuous thin layer, $< 10 \mu\text{m}$, consisting of planar grains formed in the vicinity of the substrate. This morphology evolves into columnar grains with continued solidification of the cladding. This microstructure is consistent with the results of a similar study in which martensitic stainless steel is deposited [43]. The very high thermal gradient in the contact zone of the melt pool with the cold substrate contributed to the formation of planar grains. The microstructure evolves into a colum-

nar/dendritic structure due to a rapid decrease in the thermal gradient when more material solidifies. Moreover, columnar grains grow perpendicular to the substrate/solidified material, i.e., in the opposite direction of the primary heat dissipation source, as is usual in DLD solidification [44]. As seen in Figure 7, this columnar/dendritic structure is the characteristic microstructure of the cladding.

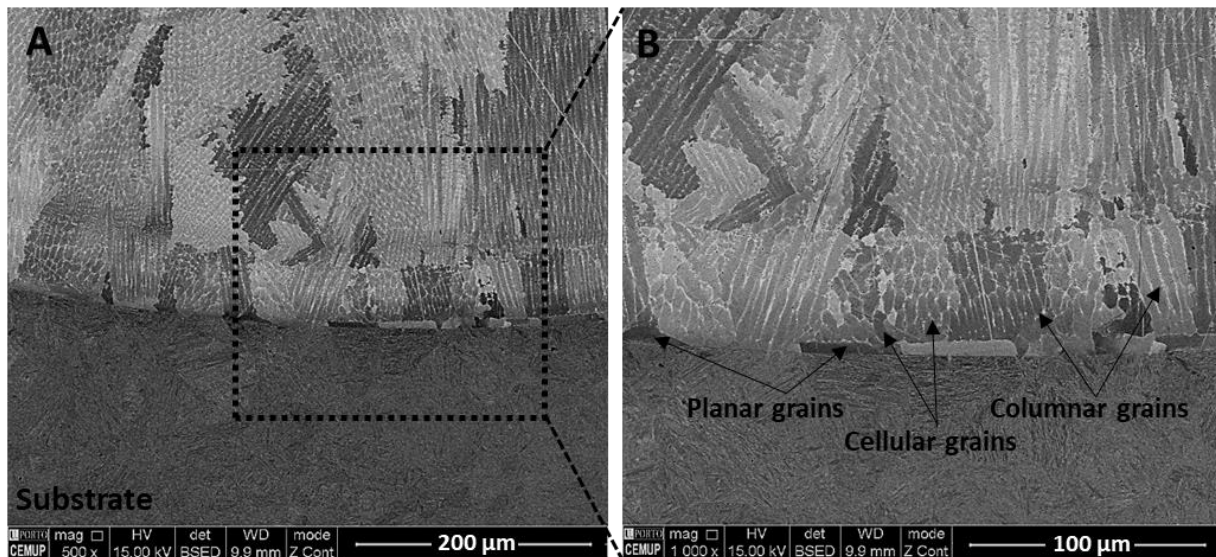


Figure 6. Microstructure of cladding produced by the I2_6_20 cladding condition on the preheated substrate, showing (A) substrate interface cladding zone. (B) A higher magnification illustration of the interface.

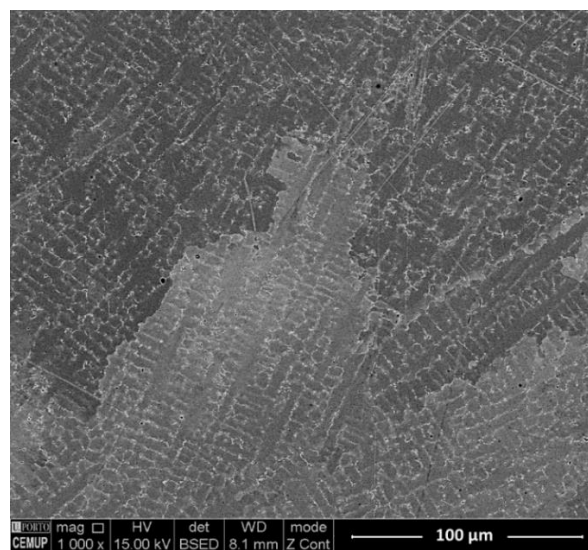


Figure 7. SEM image of the I2_6_20 cladding microstructure.

Figure 8 shows a high-magnification SEM image and elemental mapping of the microstructure of the I2_6_20 cladding. This microstructure consists of the γ matrix, bright zones (surrounded by a segregation zone), and rounded dark particles. The elemental mapping indicates that the bright zones are rich in Mo and Nb, indicating the formation of the Laves phase located at the interdendritic region. Rounded dark particles are complex oxides dispersed in the γ matrix. Table 4 shows the chemical composition obtained by EDX analysis of the zones indicated in Figure 8.

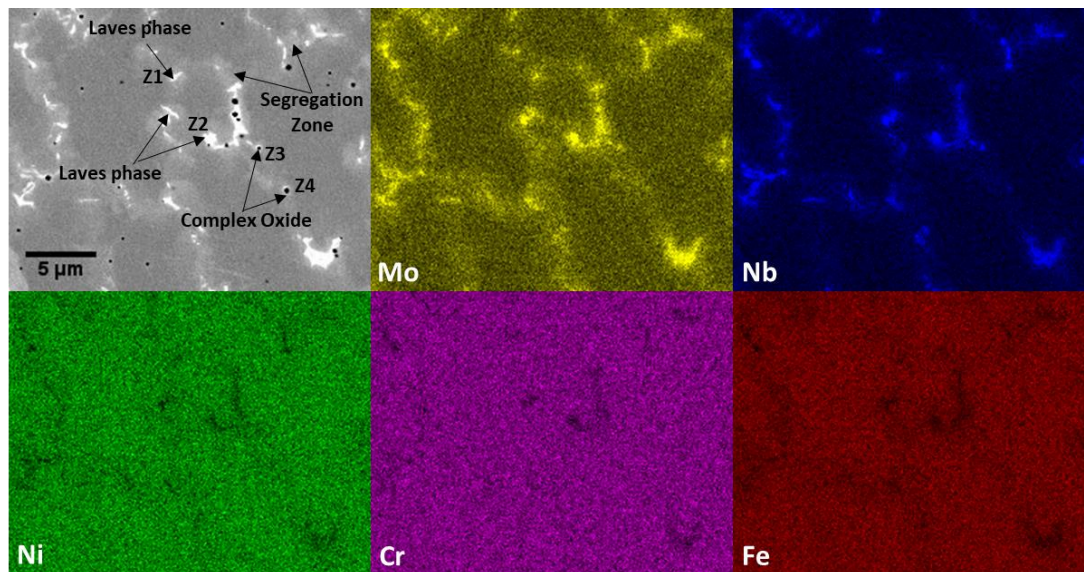


Figure 8. SEM image and the elemental maps obtained by EDX microanalysis showing segregation zones associated with the Laves phase and complex oxides.

Table 4. Chemical composition (%) of the zones indicated in Figure 8.

| Phases | Zones | Ni | Cr | Mo | Nb | Si | Fe | Mn | Al | Ca | C | O |
|-------------|-------|-------|-------|-------|-------|-------|-------|------|-------|------|------|-------|
| Laves phase | Z1 | 42.16 | 17.39 | 10.97 | 10.88 | 3.17 | 15.43 | - | - | - | - | - |
| | Z2 | 42.29 | 17.91 | 10.62 | 10.34 | 2.63 | 16.21 | - | - | - | - | - |
| Oxide | Z3 | 0.33 | 4.24 | - | 1.11 | 13.00 | - | 2.44 | 15.83 | 4.70 | 2.58 | 55.77 |
| | Z4 | 0.71 | 4.38 | - | 1.18 | 14.71 | - | 1.78 | 14.58 | 6.91 | - | 55.75 |

The γ dendrites are formed during the solidification of nickel-based superalloys processed by DLD, segregating Nb and Mo into the liquid, thus creating the local conditions for forming the Laves phase. The final stage of non-equilibrium solidification thus gives rise to this microstructure consisting mainly of the γ matrix and Laves phase. A similar microstructure has been found in other nickel-based superalloy solidification studies [45–51].

Laves phase formation promotes the initiation and propagation of cracks, with a detrimental effect in mechanical response, reducing ductility, ultimate tensile strength, fracture resistance, and fatigue life [52,53]. Thus, this phase reduces the performance of Inconel 625, requiring control of morphology and distribution in the cladding.

A similar analysis was performed at the cladding/substrate interface, Figure 9. In the continuous thin layer adjacent to the substrate, characterized by planar grains (see Figure 6), the thermal gradient and growth rate are significantly different from those of the dendritic region, and the Laves phase was not detected.

Figure 9 shows that DLD deposition of M625 on the 42CrMo4 substrate led to cladding with a flat interface, with a thin continuous layer of planar γ grains, followed by γ dendrites and a dispersed Laves phase. As already mentioned, the appearance of the Laves phase in this region has a detrimental effect and should be minimized. Therefore, another cladding was performed with the substrate preheated to 300 °C. This procedure leads to a decrease in the thermal gradient of the deposited layer, influencing the microstructure. Preheating (PHT) increases the interdiffusion of constituents of M625 and 42CrMo4 at the bonding interface and, by decreasing the substrate cooling rate, can also affect the microstructure and properties in the heat-affected zone.

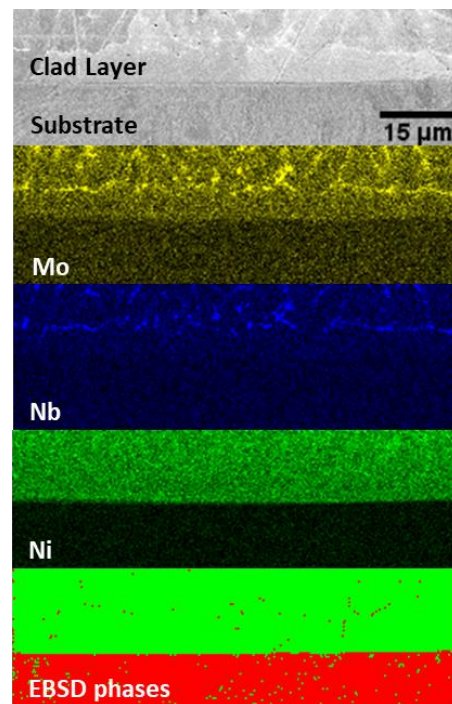


Figure 9. SEM image and elemental maps obtained by EDX microanalysis of M625 deposited on 42CrMo4 substrate. An EBSD image shows the phase distribution in this region: FCC phases in green and BCC phases in red.

The influence of PHT application on the cladding/substrate interface is shown in Figure 10. The thin layer of planar grains was not formed. Substrate heating significantly reduced the thermal gradient in the initial solidification phase of the melt pool, leading to the formation of dendrites throughout the cladding. Furthermore, it appears that PHT slightly increases the interdendritic spacing from 5–7 μm to 6–9 μm, measured by ImageJ software in Figure 6 and Figure 10, respectively. This observation confirms the decrease in the cooling rate allowing the growth of the interdendritic spacing. This feature is consistent with a study that indicates that lower cooling rates promote dendrite growth and decrease cellular grain formation in the initial stages of solidification [54].

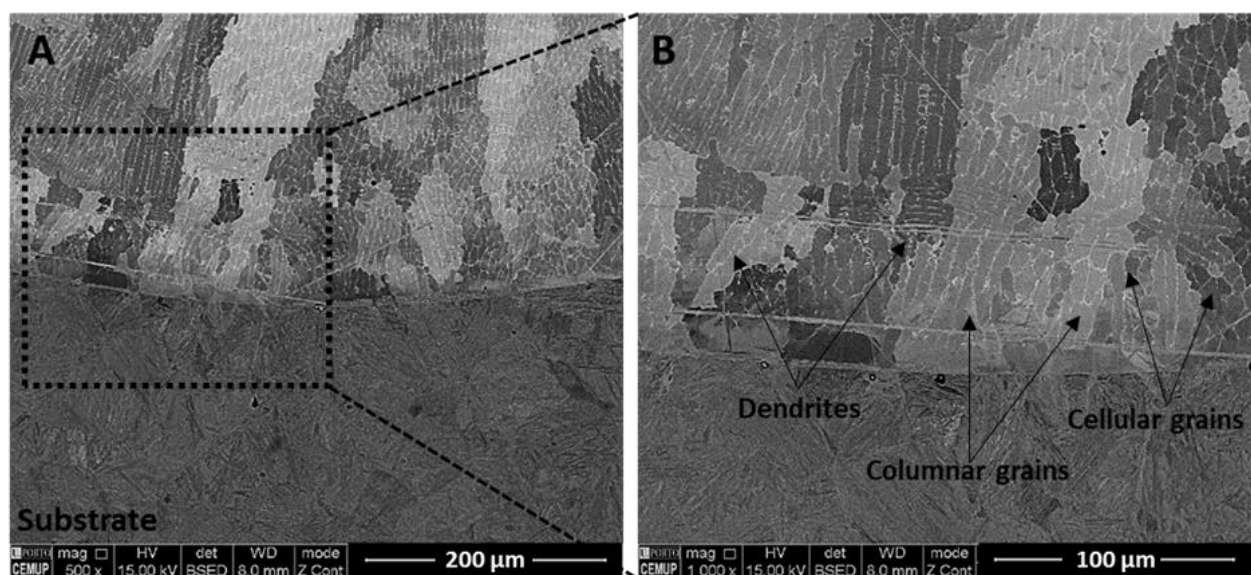


Figure 10. Microstructure of cladding produced by the I2_6_20 cladding condition on the preheated substrate, showing (A) substrate interface cladding zone. (B) A higher magnification illustration of the interface.

Besides, the application of PHT has led to the reduction in Laves phases, this effect highlighted at the interface zone, as seen in Figure 11. A lower cooling rate effectively maintained the Nb and Mo in the γ matrix, avoiding segregation. Moreover, the elemental mapping and EBSD image in Figure 11 confirm a more intense interdiffusion at the interface, which is not as plane as it was without PHT, Figure 9. Diffusion of nickel, which is a gamma-phase stabilizer, to steel is associated with a greater amount of residual austenite in this region. Thus, the application of preheating seems helpful for reducing the deleterious Laves phase and for enhancing metallurgical bonding.

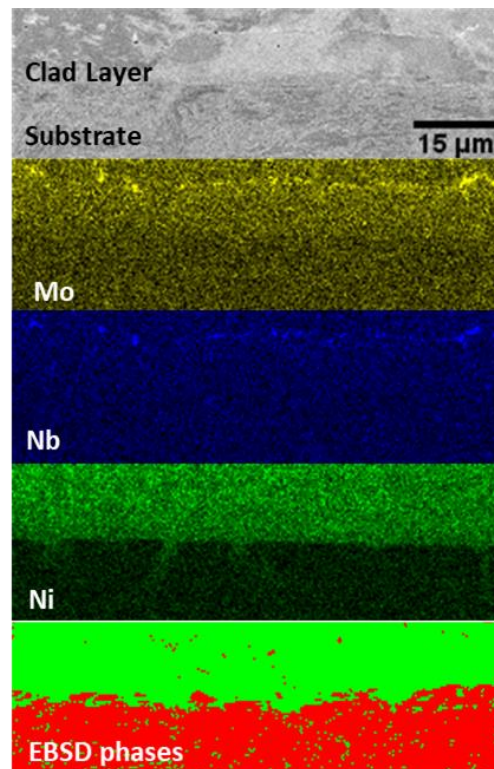


Figure 11. SEM image and elemental maps obtained by EDX microanalysis of M625 deposited on preheated (PHT) 42CrMo4 substrate. An EBSD image shows the phase distribution in this region: FCC phases in green and BCC phases in red.

The HAZ of 42CrMo4 steel is also a critical region, as substrate heating by the laser followed by rapid cooling leads to martensite formation, which can create cracks and allow for rapid crack propagation. Microstructural differences in HAZ caused by PHT were analysed by EBSD, as illustrated in Figure 12. This figure shows that PHT affects the HAZ microstructure, with larger (longer and wider) martensite laths caused by a slower cooling rate. Martensite with wider laths is associated with lower mechanical strength which, together with the more significant amount of residual austenite determined when using PHT, can reduce the brittleness of this region.

Figure 12 also shows that no preferential crystalline orientation was formed in the HAZ of claddings without or with PHT.

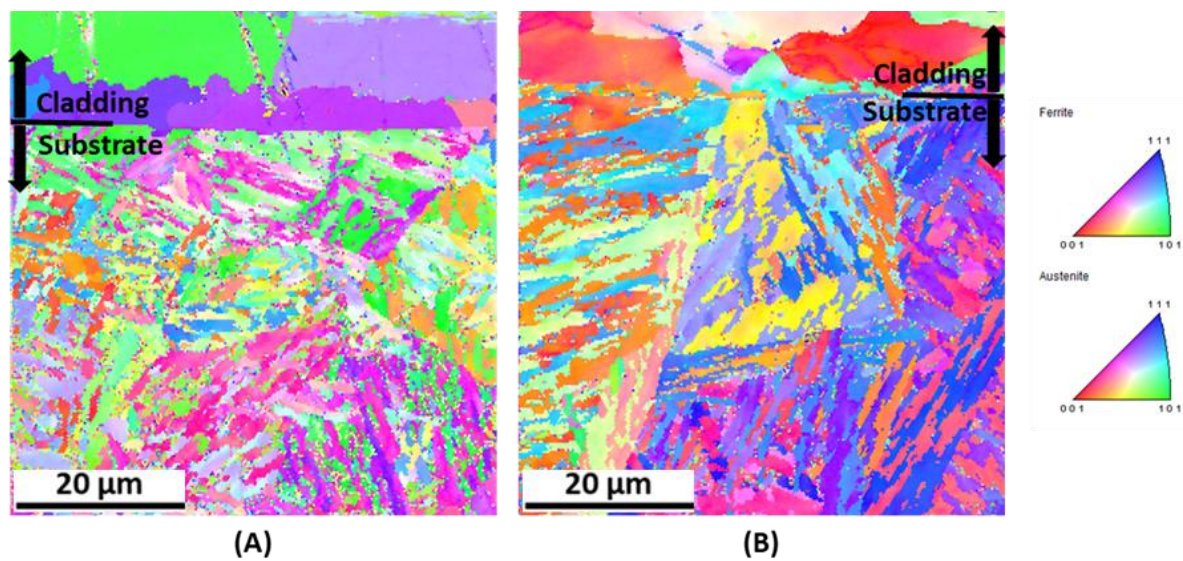


Figure 12. EBSD images of the I2_6_20/cladding interface region. (A) Without PHT; (B) with PHT.

3.3. Microhardness Measurements

The microhardness profile shown in Figure 13 shows that the hardness distribution in the cladding zone is uniform and independent of PHT, with an average hardness of 258 ± 2 HV and 253 ± 2 HV for the samples with and without preheating, respectively. A sharp transient zone with a pronounced hardness increase is measured in the HAZ of the sample without PHT (maximum hardness of 491 ± 23 HV). The application of PHT to the substrate before deposition produced a more uniform distribution of hardness in the HAZ (368 ± 25 HV), with a less sharp transient near the interface. Furthermore, the hardness peak has been eliminated, and the hardness values show less dispersion. These differences in hardness are attributed to changes in the microstructure induced by PHT, as seen in Figure 12, and its influence on chemical composition distribution, seen in Figures 9 and 11, and indicate that the HAZ region is less prone to cracking.

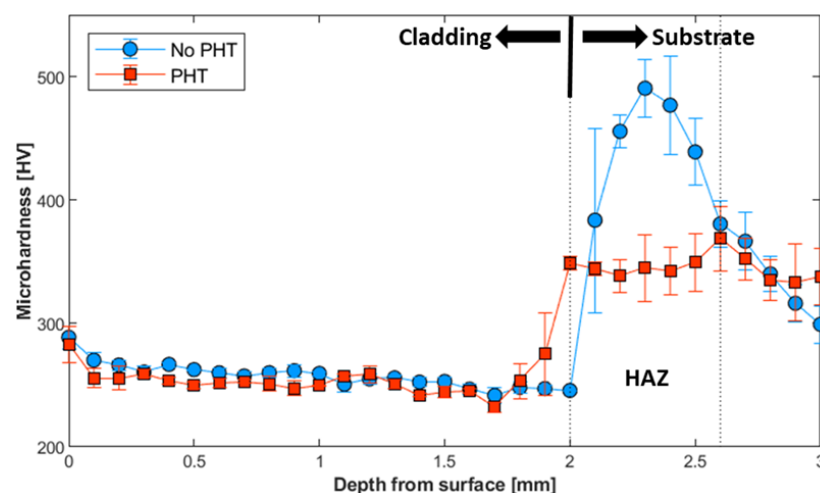


Figure 13. Microhardness profile of cladded samples applying the I2_6_20 condition with and without PHT.

4. Conclusions

The deposition of Inconel 625 claddings onto a 42CrMo4 steel substrate was performed using direct laser deposition (DLD) and varying processing conditions: laser power, scan-

ning speed, feed rate, and preheating. Macro- and microstructural analysis, in addition to the hardness measurements, led to the following main conclusions:

- A DLD process window map considering processing variables shows that several combinations can be used. However, the cladding produced with 2 kW of laser power, a scanning speed of 6 mm/s, and a 20 g/min feed rate presented adequate dilution and wettability.
- The deposited layers were produced without significant structural defects such as cracks, pores, or other types of discontinuities.
- Substrate preheating to 300 °C influences the microstructure of the cladding/substrate interface, reducing the formation of the deleterious Laves phase.
- PHT also alters the hardness profile, mainly in the heat-affected zone, due to modification of the martensite microstructure and increased residual austenite.

Author Contributions: A.A.F., M.F.V., and A.R.R. proposed the methodology and results data analyses followed in this research; A.A.F., J.M.C., P.C.R., and R.L.A. carried out the experimental tests. All authors participated in the discussion of results and writing of the manuscript. All authors have read and agreed to the published version of the manuscript.

Funding: This research was funded by FEDER through the Operational Programme for Competitiveness and Internationalization (COMPETE 2020), Projetos em Copromoção (project POCI-01-0247-FEDER-039848).

Institutional Review Board Statement: Not applicable.

Informed Consent Statement: Not applicable.

Data Availability Statement: Not applicable.

Acknowledgments: The authors give their thanks to the CEMUP (Centro de Materiais da Universidade do Porto) for expert assistance with SEM.

Conflicts of Interest: The authors declare no conflict of interest.

References

1. Bian, L.; Shamsaei, N.; Usher, J.M. *Laser-Based Additive Manufacturing of Metal Parts*, 1st ed.; CRC Press: Boca Raton, FL, USA, 2018.
2. Ur Rahman, N.; Matthews, D.T.; de Rooji, M.; Khorasani, A.M.; Gibson, I.; Cordova, L.; Römer, G. An Overview: Laser-Based Additive Manufacturing for High Temperature Tribology. *Front. Mech. Eng.* **2019**, *5*, 1–15. [[CrossRef](#)]
3. Thompson, S.M.; Bian, L.; Shamsaei, N.; Yadollahi, A. An overview of Direct Laser Deposition for additive manufacturing; Part I: Transport phenomena, modeling and diagnostics. *Addit. Manuf.* **2015**, *8*, 36–62. [[CrossRef](#)]
4. Song, L.; Bagavath-Singh, V.; Dutta, B.; Mazumder, J. Control of melt pool temperature and deposition height during direct metal deposition process. *Int. J. Adv. Manuf. Technol.* **2012**, *58*, 247–256. [[CrossRef](#)]
5. Petrat, T.; Graf, B.; Gumenyuk, A.; Rethmeier, M. Laser metal deposition as repair technology for a gas turbine burner made of inconel 718. *Phys. Procedia* **2016**, *83*, 761–768. [[CrossRef](#)]
6. Alimardani, M.; Fallah, V.; Khajepour, A.; Toyserkani, E. The effect of localised dynamic surface preheating in laser cladding of Stellite 1. *Surf. Coatings Technol.* **2010**, *204*, 3911–3919. [[CrossRef](#)]
7. Leunda, J.; García Navas, V.; Soriano, C.; Sanz, C. Effect of laser tempering of high alloy powder metallurgical tool steels after laser cladding. *Surf. Coatings Technol.* **2014**, *259*, 570–576. [[CrossRef](#)]
8. Dass, A.; Moridi, A. State of the art in directed energy deposition: From additive manufacturing to materials design. *Coatings* **2019**, *9*, 418. [[CrossRef](#)]
9. Lahrou, Y.; Brissaud, D. A Technical Assessment of Product/Component Re-manufacturability for Additive Remanufacturing. *Procedia CIRP* **2018**, *69*, 142–147. [[CrossRef](#)]
10. Kush, M. *Advanced Manufacturing Technologies Modern Machining Advanced Joining Sustainable Manufacturing*; Springer International Publishing: New York, NY, USA, 2018; p. 294. [[CrossRef](#)]
11. Pinkerton, A.J.; Wang, W.; Li, L. Component repair using laser direct metal deposition. *Proc. Inst. Mech. Eng. B J. Eng. Manuf.* **2008**, *222*, 827–836. [[CrossRef](#)]
12. Vilar, R.; Almeida, A. Repair and manufacturing of single crystal Ni-based superalloys components by laser powder deposition—A review. *J. Laser Appl.* **2015**, *27*, S17004. [[CrossRef](#)]
13. Abioye, T.E.; McCartney, D.G.; Clare, A.T. Laser cladding of Inconel 625 wire for corrosion protection. *J. Mater. Process. Technol.* **2015**, *217*, 232–240. [[CrossRef](#)]
14. Marchese, G.; Colera, X.G.; Calignano, F.; Lorusso, M.; Biamino, S.; Minetola, P.; Manfredi, D. Characterization and Comparison of Inconel 625 Processed by Selective Laser Melting and Laser Metal Deposition. *Adv. Eng. Mater.* **2017**, *19*, 1–9. [[CrossRef](#)]

15. Gonzalez, J.A.; Mireles, J.; Stafford, S.W.; Perez, M.A.; Terrazas, C.A.; Wicker, R.B. Characterization of Inconel 625 fabricated using powder-bed-based additive manufacturing technologies. *J. Mater. Process. Technol.* **2019**, *264*, 200–210. [[CrossRef](#)]
16. Long, Y.T.; Nie, P.L.; Li, Z.G.; Huang, J.; Li, X.; Xu, X.M. Segregation of niobium in laser cladding Inconel 718 superalloy. *Trans. Nonferrous Met. Soc. China* **2016**, *26*, 431–436. [[CrossRef](#)]
17. Xiao, H.; Li, S.; Han, X.; Mazumder, J.; Song, L. Laves phase control of Inconel 718 alloy using quasi-continuous-wave laser additive manufacturing. *Mater. Des.* **2017**, *122*, 330–339. [[CrossRef](#)]
18. Singh, G.; Vasudev, H.; Bansal, A.; Vardhan, S.; Sharma, S. Microwave cladding of Inconel-625 on mild steel substrate for corrosion protection. *Mater. Res. Express* **2020**, *7*. [[CrossRef](#)]
19. Feng, K.; Feng, K.; Chena, Y.; Denga, P.; Li, Y.; Zhao, H.; Lu, F.; Li, R.; Jian, H.; Li, Z. Improved high-temperature hardness and wear resistance of Inconel 625 coatings fabricated by laser cladding. *J. Mater. Process. Technol.* **2017**, *243*, 82–91. [[CrossRef](#)]
20. Farahmand, P.; Kovacevic, R. Laser cladding assisted with an induction heater (LCAIH) of Ni-60%WC coating. *J. Mater. Process. Technol.* **2015**, *222*, 244–258. [[CrossRef](#)]
21. Wang, Z.; Zhao, J.; Zhao, Y.; Zhang, H.; Shi, F. Microstructure and microhardness of laser metal deposition shaping K465/stellite-6 laminated material. *Metals* **2017**, *7*, 512. [[CrossRef](#)]
22. Bennett, J.; Dudas, R.; Cao, J.; Ehmann, K.; Hyatt, G. Control of Heating and Cooling for Direct Laser Deposition Repair of Cast Iron Components. In Proceedings of the International Symposium on Flexible Automation, ISFA 2016, Cleveland, OH, USA, 1–3 August 2016.
23. The Laser Repair Process of High-Speed Gear Transmission Body with Better Wear Resistance and Higher Hardness. Patent CN106222651A, 14 December 2016.
24. Sadhu, A.; Choudhary, A.; Sarkar, S.; Nair, A.M.; Nayak, P.; Pawar, S.D.; Muvvala, G.; Pal, S.K.; Nath, A.K. A study on the influence of substrate preheating on mitigation of cracks in direct metal laser deposition of NiCrSiBC-60%WC ceramic coating on Inconel 718. *Surf. Coatings Technol.* **2020**, *389*, 125646. [[CrossRef](#)]
25. Shim, D.S.; Baek, D.S.; Lee, S.B.; Yu, J.H.; Choi, Y.S.; Park, S.H. Influence of heat treatment on wear behavior and impact toughness of AISI M4 coated by laser melting deposition. *Surf. Coatings Technol.* **2017**, *328*, 219–230. [[CrossRef](#)]
26. He, W.; Shi, W.; Li, J.; Xie, H. In-situ monitoring and deformation characterisation by optical techniques; part I: Laser-aided direct metal deposition for additive manufacturing. *Opt. Lasers Eng.* **2019**, *122*, 74–88. [[CrossRef](#)]
27. Sun, C.; Fu, P.X.; Liu, H.W.; Liu, H.H.; Du, N.Y. Effect of tempering temperature on the low temperature impact toughness of 42CrMo4-V steel. *Metals* **2018**, *8*, 232. [[CrossRef](#)]
28. *Steels and Nickel Alloys for Fasteners with Specified Elevated and/or Low Temperature*; BSISstandard: London, UK, 2013; ISBN 978 0 580 76784 5.
29. Engler, O.; Randle, V. *Introduction to texture analysis: Macrotecture, Microtexture and Orientation Mapping*, 2nd ed.; CRC Press: Boca Raton, FL, USA, 2010.
30. Abioye, T.E.; Folkes, J.; Clare, A.T. A parametric study of Inconel 625 wire laser deposition. *J. Mater. Process. Technol.* **2013**, *213*, 2145–2151. [[CrossRef](#)]
31. Toyserkani, E.; Khajepour, A.; Corbin, S. *Laser Cladding*, 1st ed.; CRC Press: Boca Raton, FL, USA, 2004.
32. Li, C.; Guo, Y.B.; Zhao, J.B. Interfacial phenomena and characteristics between the deposited material and substrate in selective laser melting Inconel 625. *J. Mater. Process. Technol.* **2017**, *243*, 269–281. [[CrossRef](#)]
33. Ferreira, A.A.; Darabi, R.; Sousa, J.P.; Cruz, J.M.; Reis, A.R.; Vieira, M.F. Optimization of direct laser deposition of a martensitic steel powder (Metco 42c) on 42CrMo4 steel. *Metals* **2021**, *11*, 672. [[CrossRef](#)]
34. Emamian, A.; Corbin, S.F.; Khajepour, A. In-Situ Deposition of Metal Matrix Composite in Fe-Ti-C System Using Laser Cladding Process. *Met. Ceram. Polym. Compos. Var. Uses* **2011**. [[CrossRef](#)]
35. Farshidianfar, M.H.; Khajepour, A.; Gerlich, A.P. Effect of real-time cooling rate on microstructure in Laser Additive Manufacturing. *J. Mater. Process. Technol.* **2016**, *231*, 468–478. [[CrossRef](#)]
36. Emamian, A.; Corbin, S.F.; Khajepour, A. Effect of laser cladding process parameters on clad quality and in-situ formed microstructure of Fe-TiC composite coatings. *Surf. Coatings Technol.* **2010**, *205*, 2007–2015. [[CrossRef](#)]
37. Ocelik, V.; de Oliveira, U.; de Boer, M.; de Hosson, J.T.M. Thick Co-based coating on cast iron by side laser cladding: Analysis of processing conditions and coating properties. *Surf. Coatings Technol.* **2007**, *201*, 5875–5883. [[CrossRef](#)]
38. de Oliveira, U.; Ocelik, V.; De Hosson, J.T.M. Analysis of coaxial laser cladding processing conditions. *Surf. Coatings Technol.* **2005**, *197*, 127–136. [[CrossRef](#)]
39. Liu, J.; Li, J.; Cheng, X.; Wang, H. Effect of dilution and macrosegregation on corrosion resistance of laser clad AerMet100 steel coating on 300M steel substrate. *Surf. Coatings Technol.* **2017**, *325*, 352–359. [[CrossRef](#)]
40. Le, T.N.; Lo, Y.L. Effects of sulfur concentration and Marangoni convection on melt-pool formation in transition mode of selective laser melting process. *Mater. Des.* **2019**, *179*, 107866. [[CrossRef](#)]
41. Marya, M.; Singh, V.; Hascoet, J.-Y.; Marya, S. Metallurgical Investigation of the Direct Energy Deposition Surface Repair of Ferrous Alloys. *J. Mater. Eng. Perform.* **2018**, *27*, 813–824. [[CrossRef](#)]
42. Ocelik, V.; Hemmati, I.; De Hosson, J.T.M. The influence of processing speed on the properties of laser surface deposits. *Surf. Contact Mech. Incl. Tribol. XII* **2015**, *1*, 93–103. [[CrossRef](#)]
43. Hemmati, I.; Ocelik, V.; De Hosson, J.T.M. Microstructural characterisation of AISI 431 martensitic stainless steel laser-deposited coatings. *J. Mater. Sci.* **2011**, *46*, 3405–3414. [[CrossRef](#)]

44. Dinda, G.P.; Dasgupta, A.K.; Mazumder, J. Laser aided direct metal deposition of Inconel 625 superalloy: Microstructural evolution and thermal stability. *Mater. Sci. Eng. A* **2009**, *509*, 98–104. [[CrossRef](#)]
45. Naghiyan Fesharaki, M.; Shoja-Razavi, R.; Mansouri, H.A.; Jamali, H. Microstructure investigation of Inconel 625 coating obtained by laser cladding and TIG cladding methods. *Surf. Coatings Technol.* **2018**, *353*, 25–31. [[CrossRef](#)]
46. Xiao, H.; Li, S.M.; Xiao, W.J.; Li, Y.Q.; Cha, L.M.; Mazumder, J.; Song, L.J. Effects of laser modes on Nb segregation and Laves phase formation during laser additive manufacturing of nickel-based superalloy. *Mater. Lett.* **2017**, *188*, 260–262. [[CrossRef](#)]
47. Knorovsky, G.A.; Cieslak, M.J.; Headley, T.J. Inconel 718 A Solidification Diagram. *Metall. Transactions A* **1989**, *20*, 2149–2158. [[CrossRef](#)]
48. Wang, L.; Dong, J.; Tian, Y.; Zhang, L. Microsegregation and Rayleigh number variation during the solidification of superalloy Inconel 718. *Mineral. Metall. Mater.* **2008**, *15*, 594–599. [[CrossRef](#)]
49. Dupont, J.N. Solidification of an Alloy 625 Weld Overlay. *Metall. Mater. Trans. A* **1996**, *27*, 3612–3620. [[CrossRef](#)]
50. Cieslak, M.J.; Headley, T.J.; Kollie, T.; Romig, A.D. A Melting and Solidification Study of Alloy 625. *Met. Mater. Trans. A* **1988**, *19*, 2319–2331. [[CrossRef](#)]
51. Nie, P.; Ojo, O.A.; Li, Z. Numerical modeling of microstructure evolution during laser additive manufacturing of a nickel-based superalloy. *Acta Mater.* **2014**, *77*, 85–95. [[CrossRef](#)]
52. Xie, H.; Yang, K.; Li, F.; Sun, C.; Yu, Z. Investigation on the Laves phase formation during laser cladding of IN718 alloy by CA-FE. *J. Manuf. Process.* **2020**, *52*, 132–144. [[CrossRef](#)]
53. Chen, Y.; Guo, Y.; Xu, M.; Ma, C.; Zhang, Q.; Wang, L.; Yao, J.; Li, Z. Study on the element segregation and Laves phase formation in the laser metal deposited IN718 superalloy by flat top laser and gaussian distribution laser. *Mater. Sci. Eng. A* **2019**, *754*, 339–347. [[CrossRef](#)]
54. Porter, D.A.; Easterling, K.E.; Sherif, M.Y. *Phase Transformations in Metals and Alloys*, 3rd ed.; CRC Press: Boca Raton, FL, USA, 2009.